PCCP

PAPER

View Article Online
View Journal | View Issue

Cite this: *Phys. Chem. Chem. Phys.*, 2015, **17**, 15173

Co-electrodeposition of RuO_2–MnO_2 nanowires and the contribution of RuO_2 to the capacitance increase†

Zhe Gui, Eleanor Gillette, Jonathon Duay, Junkai Hu, Nam Kim and Sang Bok Lee*

Received 27th March 2015,
Accepted 29th April 2015

DOI: 10.1039/c5cp01814e

www.rsc.org/pccp

A wide range of metal oxides have been studied as pseudocapitors, with the goal of achieving higher power than traditional batteries and higher energy than traditional capacitors. However, most metal oxides have relatively low conductivity, and the few exceptions, like RuO_2, are prohibitively expensive. Mixed metal oxides provided an opportunity to incorporate small amounts of expensive materials to enhance the performance of a less expensive, poorer performing material. Here, by homogeneously co-depositing a small amount of energy dense and conductive RuO_2 into MnO_2 nanowires, we demonstrate an improvement in specific capacitance. Importantly, we also demonstrate that this improvement is not primarily provided by redox activity of RuO_2, but rather by improvement of the composite conductivity. A series of RuO_2–MnO_2 composite nanowires with different RuO_2 loading percentages have been synthesized by performing co-electrodeposition in a porous alumina template. The structure of these RuO_2–MnO_2 nanowires is characterized by TEM and SEM. EDS mapping shows that RuO_2 is well distributed in MnO_2 matrix nanowires. The chemical constituents and the phase of these composite nanowires are confirmed by X-ray photoelectron and Raman spectroscopy. The amount of RuO_2 is controlled by varying the concentrations of $RuCl_3$ and $MnAc_2$ in the deposition solution. The precise masses of MnO_2 and RuO_2 are determined by ICP-AES elemental analysis. MnO_2 nanowires with 6.70 wt% RuO_2 demonstrate a specific capacitance of 302 F g^{-1} at 20 mV s^{-1}, compared to 210 F g^{-1} for pristine MnO_2 nanowires. Investigation of the RuO_2 loading amount effect was conducted by electrochemical impedance spectroscopy (EIS) and deconvolution of capacitances, using methods previously reported by both Dunn and Transsiti. The RuO_2–MnO_2 nanowires studied here demonstrate a simple, straighforward method to overcome the intrinsically poor conductivity of MnO_2, and clarify the source of RuO_2's contribution to the improved performance.

Introduction

Composite materials have been broadly used to improve the performance of metal oxides for supercapacitors, generally for the purpose of increasing the surface area or conductivity.

Composites and heterogeneous structures using MnO_2 are common due to their abundance, low cost, and environmental friendliness.[1] However, their performance is ultimately limited by their intrinsically poor electrical conductivity of 10^{-5} to 10^{-6} S cm^{-1}, so they benefit from increased conductivity using a conductive scaffolding or using additives.[2–5] Well-ordered 1D nanoarrays and 3D porous structures of MnO_2, synthesized by using templates (AAO) or nanostructured current collectors (metal arrays and 3D porous metals), have been reported to show superior electrochemical and mechanical properties over their bulk counterparts.[6–9] A more effective method is to integrate MnO_2 into conductive components with precise control, resulting in sophisticated architectures, *e.g.* MnO_2/CNT coaxial nanotubes[10] and MnO_2 wrapped with graphene or CNT.[11,12] In this approach, conductive supplementary materials are added either before MnO_2 growth or through additional layer, coating, or wrapping methods after MnO_2 synthesis.[13–16] However, an alternative approach is to create heterogeneous composites with other metal oxides, which has the advantage of relatively straightforward processing and a wider range of performance enhancing properties to choose from.[17–21] Different metal oxides including Ni,[17,19] Fe,[22] Co,[19] V,[21,23] Mo,[20] Ru,[24] and Cu[25] oxides have been reported. Some of these metal oxides show improved conductivity while others show better stability.

Ru oxide is of particular interest because of its impressive theoretical capacitance. $RuO_2 \cdot xH_2O$ has mixed ionic and electrical

Department of Chemistry and Biochemistry, University of Maryland, College Park, MD 20740, USA. E-mail: slee@umd.edu

† Electronic supplementary information (ESI) available: TEM, XPS and charge deconvoluted cyclic voltammetry. See DOI: 10.1039/c5cp01814e

conductivities and is known to exhibit a high specific capacitance as well as excellent high power performance.[26] However, due to its high cost, its applications have been limited mostly to military and aerospace. RuO_2 also requires an acidic electrolyte (H_2SO_4), which is not considered to be environmentally friendly and severely restricts the potential application of RuO_2 itself in energy storage devices. Therefore, a more efficient utilization of RuO_2 is desired for its application in energy storage. RuO_2 has been reported previously to couple with MnO_2 as an energy storage material for supercapacitors using a variety of synthesis methods.[24,27,28] For example, electrospinning has been utilized to produce MnO_2–RuO_2 nanofiber mats, resulting in a capacitance of 208 F g^{-1} at 10 mV s^{-1}.[24] Oxidative co-precipitation of MnO_2 and RuO_2 was also reported to exhibit a high specific capacitance of 273 F g^{-1} with 9 wt% RuO_2 at 200 mA g^{-1}; however, acetylene black (20 wt%) added in the electrode preparation also contributes partially to this high specific capacitance.[27] In this paper, we achieved the mixing of MnO_2 and RuO_2 homogenously, at the nanoscale, and even with a relatively low loading amount of RuO_2, we successfully improved the composite conductivity and allowed a higher efficiency utilization of MnO_2. Additionally, we clearly identified the contributions of each component to the performance enhancement, which is critical for the rational design of composite materials. This work introduces a simple, promising approach to improve the poor conductivity of MnO_2 for better supercapacitor performance by using a small amount of RuO_2, which may also be applied to synthesize many other ceramic hybrid structures for synergistic properties. The RuO_2 (<10 wt%) in the composites contributes some capacitance through its own charge storage, but more significantly, it improves the conductivity of the composite and enhances the utilization of MnO_2. Composite MnO_2–RuO_2 nanowire arrays are synthesized without any other additives by a simple one-step electrochemical co-deposition method, resulting in uniform and homogeneous hybrid nanowire arrays. The higher conductivity in the composite sample is demonstrated by electrochemical impedance spectroscopy (EIS) characterization results. A high specific capacitance of 302 F g^{-1} was obtained with only 6.70 wt% RuO_2. A detailed analysis of the RuO_2 contribution is carried out for a variety of RuO_2 mass loading amounts. Samples with higher amounts of RuO_2 show higher capacitances, and by deconvoluting the capacitance of samples with increasing RuO_2 amounts, we found that the capacitance improvement in the composite sample is mainly attributed to the increase of the surface stored charge, which is facilitated by the enhanced electrical conductivity in the composite samples, while there is less influence of the RuO_2 loading amount found on the insertion capacitance.

Experimental

Synthesis

Electrodeposition. First a layer of gold is sputtered onto the branched side of an AAO template using a Denton Vacuum Desktop III sputter machine. Copper tape (3 M) is then attached to the sputtered side of the AAO in connection with the electrical circuit. Defining and sealing of the electroactive window (0.32 cm^2) is performed using silicone rubber. The as-prepared AAO is used as the working electrode with Ag/AgCl as the reference electrode and platinum as the counter electrode during the electrodeposition process. RuO_2–MnO_2 nanowires are synthesized potentiostatically at 0.75 V in an aqueous solution of $RuCl_3$ (1–20 mM), $MnAc_2$ (20–100 mM) and NaAc (100 mM) until the charge reached 200 mC. Electrodeposition solutions were used with Ru/Mn ion ratios of 1/100, 1/20, and 1/2 having the total compositions of: 1 mM $RuCl_3$–100 mM $MnAc_2$, 1 mM $RuCl_3$–20 mM $MnAc_2$, and 10 mM $RuCl_3$–20 mM $MnAc_2$, respectively (all containing 100 mM of NaAc). The electrodeposited nanowires in the AAO template were then annealed in air at 200 °C for 1 h. The AAO template is subsequently dissolved in 3 M NaOH solution and rinsed with distilled water to obtain nanowire arrays for characterization.

Characterization

ICP-AES. Elemental analysis by the inductively coupled plasma atomic emission spectroscopy (ICP-AES) is performed using a PerkinElmer ICP-Optima 4700 to measure the masses of RuO_2 and MnO_2, which can be used to calculate the RuO_2 weight percentages and specific capacitances. Calibration curves were obtained using Ru and Mn standards traceable by the National Institute of Standards and Technology (NIST). Samples were dissolved in freshly made aqua regia solution (prepared by mixing 3 : 1 concentrated $HCl : HNO_3$) and diluted to a known volume before being administered to the plasma. Intensities of Mn at 257.610 nm and Ru at 240.272 nm were collected to obtain quantitative information of the two elements. Samples were prepared in solutions with compositions of: 1 mM $RuCl_3$–20 mM $MnAc_2$, 5 mM $RuCl_3$–20 mM $MnAc_2$, and 10 mM $RuCl_3$–20 mM $MnAc_2$.

Imaging of MnO_2 nanowires was performed using a field emission scanning electron microscope (Hitachi SU-70 FEG-SEM, operated at 5 eV) and a transmission electron microscope ((JEOL JEM 2100 FE-TEM), 200 keV).

Raman spectra were collected using a Horiba JobinYvonLabRAM Raman microscope (model ARAMIS) with excitation lines that included 532 nm and 633 nm. In these experiments, green laser line (532 nm) excitation was utilized for nanowires.

XPS. XPS analysis was done on a Kratos AXIS 165 spectrometer. The adventitious hydrocarbon C1s signal at 284.6 eV was used as the energy reference to correct charging.

Electrochemical test. The electrochemical studies of MnO_2 nanowire arrays were performed in a standard three-electrode system utilizing a bipotentiostat (BI-STAT, Princeton Applied Research). Ag/AgCl was used as the reference electrode and Pt was used as the counter electrode. Cyclic voltammetry and galvanostatic charge/discharge were performed in 1 M $NaSO_4$ with a potential window from 0–1 V *vs.* Ag/AgCl. The specific capacitance was calculated using cyclic voltammograms based on eqn (1)

$$C_{sp} = \frac{Q}{\Delta E m} \quad (1)$$

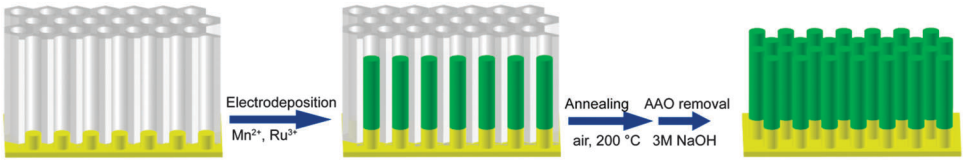

Scheme 1 Schematic illustration of the electrochemical co-deposition process.

where Q is the charge stored in the CV curve, ΔE is 1.0 V and m is the mass determined by the elemental analysis of ICP-AES. Electrochemical impedance spectroscopy was conducted in a three electrode configuration, with a frequency ranging from 100 kHz to 100 MHz at open circuit potential.

Results and discussion

Electrochemical co-deposition

Scheme 1 shows the preparation process for RuO_2–MnO_2 composite nanowire arrays. Anodic aluminum oxide (AAO) with gold sputtered on one side is used as a template. An electrolyte bath consisting of both manganese(II) ions and ruthenium(III) ions is used for deposition. After applying a constant potential of 0.75 V *vs.* Ag/AgCl, MnO_2 and RuO_2 start to co-deposit inside the AAO template and grow into nanowires. After electrodeposition, the nanowires are annealed at 200 °C in air for 1 hour followed by the removal of the AAO template. The purpose of the annealing treatment is to convert RuO_2 into a more conductive phase.[29] The mild temperature of 200 °C chosen here can effectively improve the electrical conductivity without sacrificing the good ionic conductivity, which is known to drop dramatically when all the water in hydrated RuO_2 is removed.[30–33] It has been reported that hydrated-RuO_2 with around 0.5 H_2O/Ru will show the best performance as a supercapacitor material with both electronic and ionic conductivity being well balanced.[31] In this work, RuO_2 co-deposited in the MnO_2 nanowire matrix can facilitate fast charge transfer during the charge/discharge process while improving the capacitive performance of MnO_2 nanowires.

Structural characterization

The structure of nanowire arrays was characterized using SEM and TEM images. Fig. 1a shows the SEM image of RuO_2–MnO_2 composite nanowire arrays grown on a flat-top gold electrode after the removal of the AAO template. The nanowires are shown to aggregate due to the surface tension during the evaporation of water. A TEM image of a nanowire, around 200 nm in diameter, which corresponds to the pore size of the AAO template, is shown in Fig. 1b. In the corresponding high resolution TEM (HRTEM) image (Fig. 1c), crystals with sizes around 5 nm are found. These crystals are formed rapidly over time during TEM measurements (in a few seconds) and the formation is likely due to the electron beam annealing effect.[34,35] Average d-spacings of 0.21 nm and 0.25 nm are observed using the lattice resolved TEM images (see ESI,† Fig. S1). These fringe values correspond well to the spacing between the 200 plane and 112 plane of Birnessite MnO_2 (JCPDS No. 43-1456). EDS mapping of a segment of a single

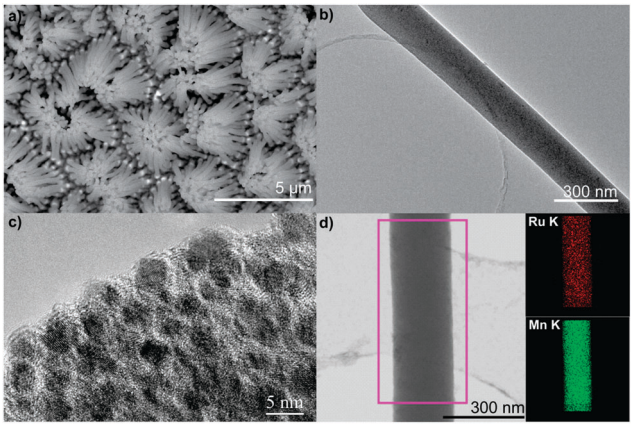

Fig. 1 (a) SEM image of RuO_2–MnO_2 composite nanowire arrays, (b) TEM image of a RuO_2–MnO_2 composite nanowire, (c) high resolution TEM (HRTEM) image of a section of a RuO_2–MnO_2 composite nanowire, and (d) TEM image (left) and EDS mappings of Ru (top right) and Mn (bottom right) on a segment of a RuO_2–MnO_2 composite nanowire.

nanowire (as indicated by the square area in Fig. 1d) was performed to confirm and locate the co-deposited RuO_2 in the MnO_2 nanowires. Almost identical mapping images of Ru and Mn signals demonstrate the homogeneous co-deposition of RuO_2 throughout the MnO_2 nanowires. This kind of architecture with conductive RuO_2 incorporated facilitates fast delivery of electrons into the MnO_2 matrix for better capacitive performance.

To confirm the chemical constituents of nanowire arrays, Raman spectroscopy and X-ray photoelectron spectroscopy were used to characterize these samples. The Raman spectra of both MnO_2 and composite nanowires are shown in Fig. 2a. For pure MnO_2, three major bands can be recognized at around 503, 576, and 652 cm^{-1}, which correspond well with Birnessite MnO_2.[36] The Raman band at 576 cm^{-1} is attributed to the (Mn–O) stretching in the basal plane of the MnO_6 sheet, while the feature at 652 cm^{-1} can be viewed as symmetric stretching vibration (Mn–O) of the MnO_6 octahedron in $MnO_2{\cdot}H_2O$. For composite samples, different Raman features are observed. Here we show three Raman spectra obtained using RuO_2–MnO_2 grown in solutions with different $RuCl_3$ concentrations. With Ru^{3+} being present in the electrodeposition bath, the peak at 652 cm^{-1} disappears and the 502 cm^{-1} peak becomes broader compared to the pure MnO_2 spectra. With increasing Ru ion concentration, the 576 cm^{-1} feature shows decreasing signal intensity. This Raman spectral change is caused by a structural distortion during RuO_2 co-deposition. A less ordered phase is formed with the addition of RuO_2, resulting in fewer features in the Raman spectra. Due to the small loading amount, RuO_2 peaks were not detected in the Raman spectra.

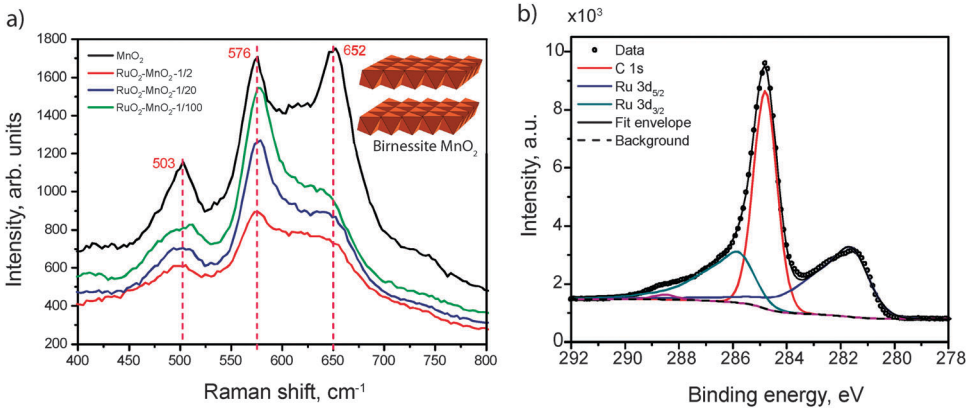

Fig. 2 (a) Raman spectra of pure MnO_2 (black curve) and RuO_2–MnO_2 prepared in solutions of different Ru/Mn ion concentration ratios (red: 1/100, blue: 1/20, green: 1/2) and (b) XPS spectra of a RuO_2–MnO_2 sample. Ru $3d_{3/2}$ (red curve) and Ru $3d_{5/2}$ (blue curve) are deconvoluted and indicated. The inset of image a shows the schematic illustration of the Birnessite MnO_2 structure.

Therefore, we used XPS to confirm the RuO_2 deposition. Fig. 2b shows the Ru 3d and C 1s spectra of RuO_2–MnO_2 composite nanowires. Although the Ru $3d_{3/2}$ spectra are obscured by the C 1s spectra, through deconvolution, we can still identify the Ru 3d doublet peaks located at the binding energy of 285.8 eV and 281.7 eV for Ru $3d_{3/2}$ and Ru $3d_{5/2}$, respectively.[37,38] The Ru 3p spectra centered at 463.2 eV further confirms the presence of RuO_2 inside MnO_2 nanowires (see ESI,† Fig. S2).

Electrochemical characterization

For the electrochemical study of RuO_2–MnO_2 nanowire arrays, we tested both pure MnO_2 nanowires and MnO_2 nanowires with 6.70% RuO_2 loading in a three-electrode system. As shown in Fig. 3a, the cyclic voltammetry curve at 100 mV s^{-1} of a composite sample demonstrates a more rectangular shape than the pure MnO_2 sample, as well as a higher total area. The square CV curve indicates a higher conductivity in the composite sample, along with an increase in total capacitance indicated by the area increase. For the pure MnO_2 nanowire arrays, the intrinsically low conductivity causes the CV curve to deviate from the rectangular shape.[39] The higher cumulative area of the CV curve for RuO_2–MnO_2 indicates a higher charge storage capability, which agrees with the galvanostatic charge/discharge results for the two samples as shown in Fig. 3b, evidenced by the longer charge/discharge time for the composite nanowires at the same current density of 1.57 mA cm^{-2}. Additionally, a smaller voltage drop (*iR* drop) was observed for the composite sample compared to the pure MnO_2, indicating a smaller resistance (R) of the RuO_2–MnO_2 sample. The CV curves of RuO_2–MnO_2 samples at different scan rates from 20–200 mV s^{-1} are shown in Fig. 3c. The square shape of the CV curve is well-maintained even at high scan rates up to 200 mV s^{-1}. This is attributed to the improved conductivity from RuO_2. Specific capacitances calculated at different scan rates from 20 to 500 mV s^{-1} for both RuO_2–MnO_2 composite and pristine MnO_2 samples are compared in Fig. 3d. The specific capacitance for pristine MnO_2 is calculated to be 210 F g^{-1} at 20 mV s^{-1}, while for composite samples, the capacitance increases by 44% to 302 F g^{-1}. At a high scan rate of 500 mV s^{-1}, the capacitance is 112 F g^{-1} for

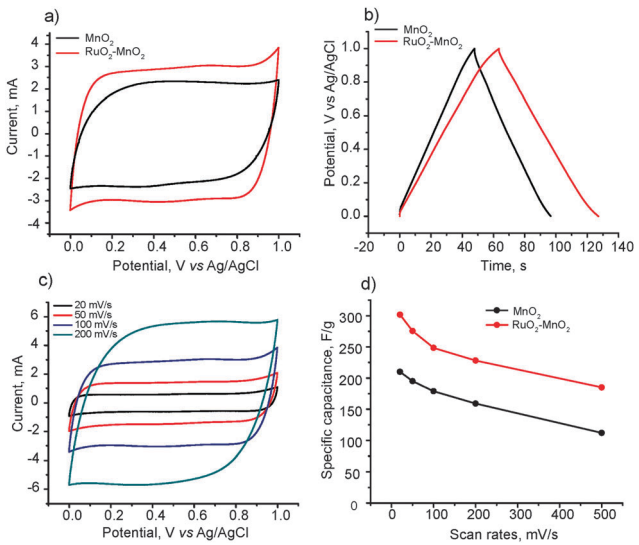

Fig. 3 (a) Cyclic voltammogram curves scanned at 100 mV s^{-1}, (b) galvanostatic curves at current density of 1.56 mA cm^{-2} of pure MnO_2 nanowires (black curves) and RuO_2 (6.70 wt%)–MnO_2 composite nanowires (red curves), (c) CV curves of RuO_2–MnO_2 at different scan rates (20–200 mV s^{-1}), and (d) specific capacitances of RuO_2 (6.70 wt%)–MnO_2 nanowires (red), and pure MnO_2 (black) measured at different scan rates. All experiments were done in 1 M Na_2SO_4 electrolyte with a potential window of 0–1 V *vs.* Ag/AgCl.

pure MnO_2 and increased by 65% to 185 F g^{-1} for composite samples. The significant improvement in capacitance, especially at high scan rates where performance is limited by the charge transfer speed, is attributed to the contribution of the co-deposited RuO_2, although it is not immediately obvious whether that contribution is primarily from the redox activity of RuO_2 itself, or through improved conductivity in the composite.[31] Therefore, both the intrinsically high capacitance and good conductivity of RuO_2 may play a role in the capacitive improvement. However, the high capacitance value for RuO_2 in the literature is usually obtained only in tests using an environmentally unfriendly acidic electrolyte. In this work, we use a neutral aqueous electrolyte

for all the electrochemical measurements. The reported value for RuO_2 in a neutral electrolyte is around 230 F g^{-1} at 20 mV s^{-1},[40] which cannot explain the high capacitance of the hybrid nanowires with a capacitance of 300 F g^{-1}. Therefore, we believe that the improved conductivity of the hybrid nanowires, rather than simply the high specific capacitance of RuO_2, is playing a crucial role in advancing the electrochemical performance. This hypothesis is supported by the more rectangular shaped CV curve of RuO_2–MnO_2 composite nanowires, as well as the smaller IR drop observed in galvanostatic testing. However, more detailed investigation of the charge transfer resistance, utilizing electrochemical impedance spectra, is discussed below to help gain insights into this composite material.

Effect of the RuO_2 loading amount

To investigate the loading amount effect of RuO_2, we prepared MnO_2 nanowire arrays with different RuO_2 amounts (0.21%, 0.56%, 2.96%, and 6.70%, calculated by ICP-AES measurements) by adjusting the solution compositions (see the Experimental part for solution concentrations and ICP-AES characterization). Fig. 5a shows the rate performance for the four samples. The specific capacitances are 235 F g^{-1}, 253 F g^{-1}, 285 F g^{-1}, and 302 F g^{-1} at 20 mV s^{-1}, and 154 F g^{-1}, 181 F g^{-1}, 206 F g^{-1}, and 228 F g^{-1} at 200 mV s^{-1} for samples with increasing loading percentages (from 0.21% to 6.70%) of RuO_2, respectively. At the same scan rate, the capacitance increased with increasing RuO_2 amounts. This phenomenon is attributed to contributions from two aspects: one is the intrinsic capacitance of RuO_2 and the other is the improved conductivity of the composite materials. If we assume that the increase in capacitance is purely a result of RuO_2's intrinsic capacitance, we can use eqn (2) to calculate the theoretical capacitance of the composite material and compare it to the experimental capacitance.

$$C_{\text{comp}} = \frac{C_{\text{MnO}_s} m_{\text{MnO}_s} + C_{\text{RuO}_s} m_{\text{RuO}_s}}{m_{\text{comp}}} \quad (2)$$

As shown in Fig. 4, the experimental capacitance of the composite is higher than the sum of the intrinsic capacitance of MnO_2 and RuO_2 alone. The disparity between the experimental and the theoretical capacitance must be the result of the synergistic properties of the composite material, allowing more of MnO_2 to be utilized.

As discussed above, both CV and GV curves indicate an improved conductivity in the RuO_2–MnO_2. To gain a deeper insight, we compare the Nyquist plots of the four samples with different RuO_2 weight percentages measured by electrical impedance spectroscopy (EIS). All four plots approximate the behavior of a transmission line model developed by Macdonald.[41] Based on the extended study of the transmission line model, important electrochemical information can be extracted from the impedance behavior at low and high frequency.[42–44] As shown in Fig. 5b, the high frequency real axis intercepts for the four samples are very close to a value around 10 ohms. This value represents the uncompensated solution resistance R_s. Therefore, all sample tested in the sample electrolyte of 1 M Na_2SO_4 have the same R_s values. The real axis impedance of the almost

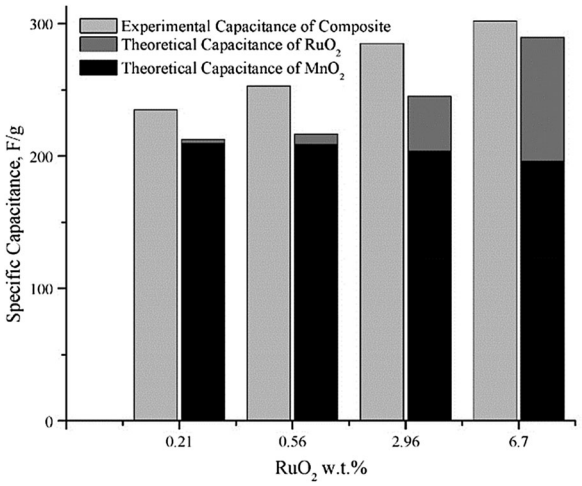

Fig. 4 Comparison of the experimental specific capacitance of the composites against the theoretical capacitance of the composite assuming that MnO_2 contributes 210 F g^{-1} measured previously, while the RuO_2 contributes its total potential contribution, based on the mass measured in the composite and a theoretical capacitance of 1400 F g^{-1}.

vertical region at low frequency indicate that the R_L equals $R_s + R_e/3$, where R_e represents the electron transfer resistance in the MnO_2 nanowires. The R_e values for the four samples are calculated and listed in the inset table in Fig. 5b. With higher RuO_2 loading percentages, the electron transfer resistance of the composite sample becomes lower. For example, the resistance of the sample with 0.21% RuO_2 is 223.8 ohm, while the one with 2.96% RuO_2 is 96.9 ohm. These EIS results confirm that the electron transfer resistance was effectively reduced by co-deposition of RuO_2 into MnO_2 nanowires. These results also explain the improving capacitive performance of the samples with increasing RuO_2 deposition amounts. With better conductivity, MnO_2 can achieve higher utilization efficiency.

Deconvolutions of the capacitance

The charge storage in MnO_2 involves two processes. One is through ion adsorption/desorption at the surface of MnO_2 and the second is through proton (H^+) or alkali metal cation (C^+) intercalation/deintercalation into the bulk MnO_2 material.[45] To explore the contribution of RuO_2 on each of these two charge storage processes, we use two methods to quantitatively discriminate the contribution of the two different processes. Deconvolutions of capacitances were conducted on both bare MnO_2 and RuO_2–MnO_2 samples with different RuO_2 percentages.

In the method developed by Trasatti,[46] voltammetric charges (q) stored at different scan rates (v) were first calculated. The extrapolation of q to $v = \infty$ of a plot of q *versus* $v^{-1/2}$ projects the charge accumulated at an infinite scan rate, which is associated with the surface stored charge, q_{cap}. The extrapolation of q^{-1} to $v = 0$ of a plot of q^{-1} *versus* $v^{1/2}$ gives the maximum charge (q_T) that can be stored in active materials, by assuming that at a slow enough scan rate all the material will be reacted. Therefore, the charge q_T equals the sum of charges stored through both processes. Subtracting q_{cap} from q_T gives the charge that is stored by the

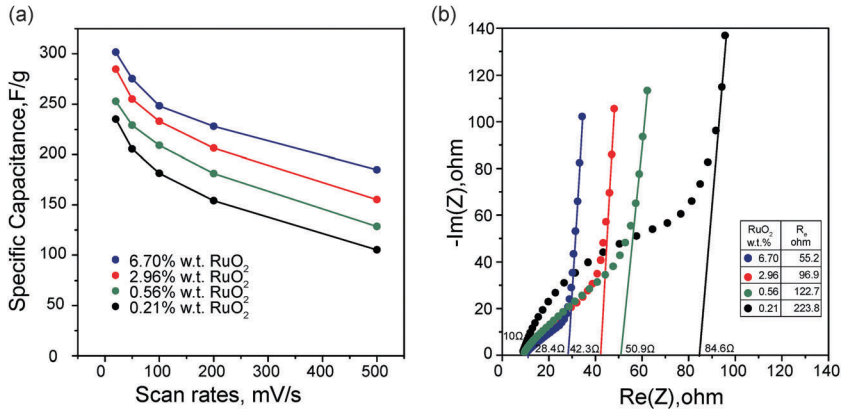

Fig. 5 (a) Specific capacitances of RuO_2–MnO_2 nanowires at different scan rates from 20 mV s^{-1} to 500 mV s^{-1}, and (b) the Nyquist plot of different samples. Four samples with different RuO_2 amounts of 0.21%, 0.56%, 2.96%, and 6.70% were prepared and tested here. The inset of image (b) shows the electrical resistance values extracted from the Nyquist plot of the four samples.

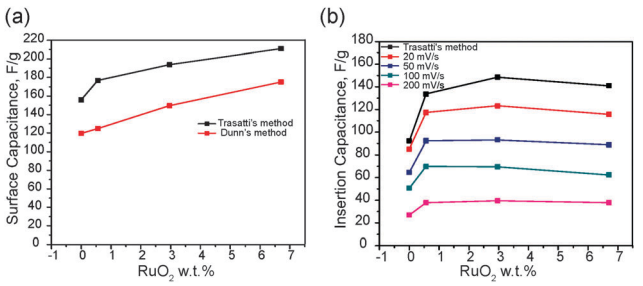

Fig. 6 Deconvolution result of the (a) capacitive capacitance, and (b) insertion capacitance of composite MnO_2 with different wt% of RuO_2.

diffusion-control insertion process, q_{in}. The corresponding specific capacitance values of q_{cap} and q_{in} can be calculated afterwards, representing the capacitive and insertion capacitance. The deconvoluted capacitive and insertion specific capacitance values for samples with different RuO_2 amounts are listed in Fig. 6a and b, respectively.

We also use the voltammetric sweep rate dependence to determine, quantitatively, the different process contributions to the current response according to a procedure reported previously by Dunn,[47] and recently used by Penner *et al.*[48] and our group.[49] The current at a certain voltage is expressed by eqn (3).

$$i = k_1 v + k_2 v^{0.5} \quad (3)$$

The term $k_1 v$ represents the current derived from the surface charge storage process, denoted as the capacitive component, while $k_2 v^{0.5}$ is associated with the diffusion controlled ion intercalation–deintercalation mechanism. To calculate the constant k_1 and k_2 values, eqn (3) is converted to eqn (4).

$$\frac{i}{v^{0.5}} = k_1 v^{0.5} + k_2 \quad (4)$$

Plots of $(i/v^{0.5})$ *versus* $v^{0.5}$ were made at a specific potential based on the voltammogram data at different scan rates to obtain the k_1 (slope) and k_2 (intercept) values. The current contributions from the surface capacitive absorption (represented by $k_1 v$ term) and diffusion-controlled insertion processes (represented by $k_2 v^{0.5}$ terms) were then deconvoluted for all samples. Based on the quantified voltammetric results (see examples in the ESI,† Fig. S3), we can determine the capacitive and insertion based capacitance values at different scan rates. The capacitive capacitances deducted from both methods for MnO_2 with different RuO_2 amounts are plotted in Fig. 6a. The capacitive capacitance shows an almost linear increase with the RuO_2 weight percentage in both Dunn's (red curve) and Trasatti's (black curve) deconvoluted results. However, for insertion capacitance, as shown in Fig. 6b, an increasing trend is found from the bare MnO_2 to the composite MnO_2 with a small loading amount of RuO_2 (0.56 wt%) in all different color curves associated with different scan rates. Typically, in the Trasatti approach (black curve in Fig. 6b), capacitance values increased from 92 F g^{-1} (for MnO_2) to 134 F g^{-1} (for RuO_2–MnO_2). With further increase in the RuO_2 amount, no significant enhancement in insertion capacitance was observed. Based on the different trends in the capacitive and insertion capacitance plots *versus* increasing RuO_2 percentages, we conclude that RuO_2 has different influences on the two charge storage processes in MnO_2. This phenomenon is explained by the different limiting factors in the two processes. The capacitive contribution is stored through the surface ion absorption/desorption. Since ions have easy access to the surface of the nanowires, electrical conductivity dominates the capacitive performance. Therefore, composite samples with higher electrical conductivity will achieve better utilization of the active materials and obtain higher capacitive capacitance. For the insertion capacitance, which is ion diffusion limited, a less significant enhancement was found with increasing RuO_2 amounts, since it only affects the electric conductivity. From the consistent charge separation results based on two methods, we confirmed that the advanced electrochemical performance demonstrated by RuO_2–MnO_2 nanowires originates from the enhancement in the material's electrical conductivity, which facilitates the capacitive charge storage process at the surface, showing an overall improved specific capacitance.

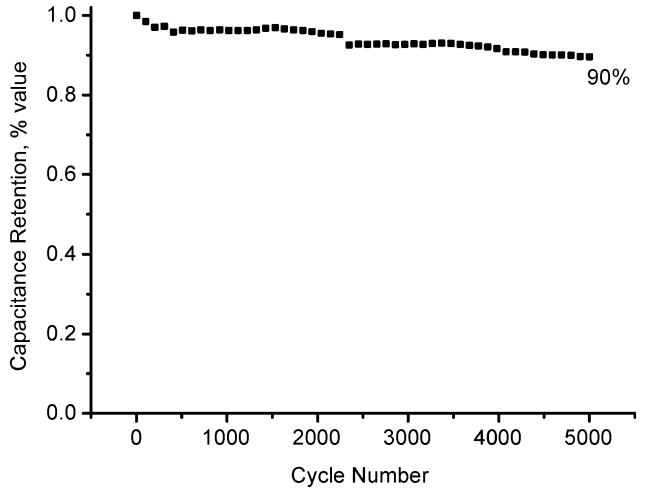

Fig. 7 Cycling test of RuO_2–MnO_2 composite nanowires up to 5k cycles.

Cycling test

Along with improved electrical conductivity and specific capacitance, composite materials also show very good cycling stability at a current density of 3 mA cm^{-2}. As shown in Fig. 7, the composite materials still maintain 90% of their initial capacitance after 5k cycles.

Conclusions

In this work, we use a one-step electrochemical co-deposition technique to obtain RuO_2–MnO_2 composite nanowires. The composite material shows a significant improvement in specific capacitance utilizing a relatively small loading amount of RuO_2 in a neutral electrolyte. Higher capacitances were found in samples with higher RuO_2 amounts, and EIS confirmed that higher RuO_2 amounts also corresponded to better conductivity. The RuO_2 contributions to the two charge storage processes in MnO_2, which either take place at the surface or in the bulk, were analyzed by two methods introduced by Trasatti and Dunn. Both capacitance separation results lead to the conclusion that RuO_2 mainly influences the capacitive capacitance that is stored through ion adsorption/desorption at the surface. This result is explained by the fact that the electron transfer limiting step in the capacitive capacitance is boosted while the ion diffusion limiting factor for the insertion capacitance is not influenced with increasing RuO_2 loading amounts. These easily prepared RuO_2–MnO_2 nanowire arrays, without any conductive additive, show promising supercapacitor performance. The synthesis method as well as the analysis of the RuO_2 amount effect can also be applied to other hybrid energy materials for a better understanding of the synergistic co-operation mechanism and further optimization of their synthesis conditions and performances.

Acknowledgements

The work was supported by the Nanostructures for Electrical Energy Storage (NEES), an Energy Frontier Research Centre (EFRC) funded by the US Department of Energy, Office of Science, Office of Basic Energy Sciences under Award Number DESC0001160. We thank Maryland Nanocenter, the Nanoscale Imaging Spectroscopy and Properties (NISP) Laboratory.

Notes and references

1 D. Bélanger, T. Brousse and J. W. Long, *Electrochem. Soc. Interface*, 2008, **17**, 49–52.
2 S. W. Zhang and G. Z. Chen, *Energy Mater. Mater. Sci. Eng. Energy Syst.*, 2008, **3**, 186–200.
3 H. Xia, M. O. Lai and L. Lu, *JOM*, 2011, **63**, 54–59.
4 W. Wei, X. Cui, W. Chen and D. Ivey, *Chem. Soc. Rev.*, 2011, **40**, 1697–1721.
5 R. Liu, J. Duay and S. B. Lee, *Chem. Commun.*, 2011, **47**, 1384–1404.
6 X. Wang, X. Wang, W. Huang, P. J. Sebastian and S. Gamboa, *J. Power Sources*, 2005, **140**, 211–215.
7 P. Yu, X. Zhang, Y. Chen and Y. Ma, *Mater. Lett.*, 2010, **64**, 61–64.
8 V. Subramanian, H. Zhu, R. Vajtai, P. M. Ajayan and B. Wei, *J. Phys. Chem. B*, 2005, **109**, 20207–20214.
9 E. Beaudrouet, A. Le Gal La Salle and D. Guyomard, *Electrochim. Acta*, 2009, **54**, 1240–1248.
10 A. L. M. Reddy, M. M. Shaijumon, S. R. Gowda and P. M. Ajayan, *Nano Lett.*, 2009, **9**, 1002–1006.
11 G. Yu, L. Hu, N. Liu, H. Wang, M. Vosgueritchian, Y. Yang, Y. Cui and Z. Bao, *Nano Lett.*, 2011, **11**, 4438–4442.
12 Z. Gui, H. Zhu, E. Gillette, X. Han, G. W. Rubloff, L. Hu and S. B. Lee, *ACS Nano*, 2013, **7**, 6037–6046.
13 J. Yan, Z. Fan, T. Wei, Z. Qie, S. Wang and M. Zhang, *Mater. Sci. Eng., B*, 2008, **151**, 174–178.
14 V. Subramanian, H. Zhu and B. Wei, *Electrochem. Commun.*, 2006, **8**, 827–832.
15 X. Dong, W. Shen, J. Gu, L. Xiong, Y. Zhu, H. Li and J. Shi, *J. Phys. Chem. B*, 2006, **110**, 6015–6019.
16 X. Lang, A. Hirata, T. Fujita and M. Chen, *Nat. Nanotechnol.*, 2011, **6**, 232–236.
17 Y.-S. Chen and C.-C. Hu, *Electrochem. Solid-State Lett.*, 2003, **6**, A210–A213.
18 T. Brousse and D. Bélanger, *Electrochem. Solid-State Lett.*, 2003, **6**, A244.
19 K. Rajendra Prasad and N. Miura, *Electrochem. Commun.*, 2004, **6**, 1004–1008.
20 M. Nakayama, A. Tanaka, Y. Sato, T. Tonosaki and K. Ogura, *Langmuir*, 2005, **21**, 5907–5913.
21 M. Nakayama, A. Tanaka, S. Konishi and K. Ogura, *J. Mater. Res.*, 2004, **19**, 1509–1515.
22 M. T. Lee, J. K. Chang, W. T. Tsai and C. K. Lin, *J. Power Sources*, 2008, **178**, 476–482.
23 M. Nakayama, M. Nishio and K. Ogura, *J. Mater. Res.*, 2003, **18**, 2364–2370.
24 T.-S. Hyun, J.-E. Kang, H.-G. Kim, J.-M. Hong and I.-D. Kim, *Electrochem. Solid-State Lett.*, 2009, **12**, A225–A228.
25 J. J. Xu, J. Yang and G. Jain, *Electrochem. Solid-State Lett.*, 2002, **5**, A223–A226.

26 D. Galizzioli, F. Tantardini and S. Trasatti, *J. Appl. Electrochem.*, 1974, **4**, 57–67.
27 J. Wen, X. Ruan and Z. Zhou, *J. Phys. Chem. Solids*, 2009, **70**, 816–820.
28 Z. Gui, J. Duay, J. Hu and S. B. Lee, *Phys. Chem. Chem. Phys.*, 2014, **16**, 12332.
29 J. M. Fletcher, W. E. Gardner, B. F. Greenfield, M. J. Holdoway and M. H. Rand, *J. Chem. Soc. A*, 1968, 653.
30 C. N. Chervin, A. M. Lubers, J. W. Long and D. R. Rolison, *J. Electroanal. Chem.*, 2010, **644**, 155–163.
31 D. A. Mckeown, P. L. Hagans, L. P. L. Carette, A. E. Russell, K. E. Swider and D. R. Rolison, *J. Phys. Chem. B*, 1999, **103**, 4825–4832.
32 W. C. Fang, J. H. Huang, L. C. Chen, Y. L. O. Su and K. H. Chen, *J. Power Sources*, 2006, **160**, 1506–1510.
33 C.-C. Hu, W.-C. Chen and K.-H. Chang, *J. Electrochem. Soc.*, 2004, **151**, A281.
34 R. F. Egerton, P. Li and M. Malac, *Micron*, 2004, **35**, 399–409.
35 I. Perez, E. Robertson, P. Banerjee, L. Henn-Lecordier, S. J. Son, S. B. Lee and G. W. Rubloff, *Small*, 2008, **4**, 1223–1232.
36 C. Julien, M. Massot, R. Baddour-Hadjean, S. Franger, S. Bach and J. P. Pereira-Ramos, *Solid State Ionics*, 2003, **159**, 345–356.
37 C. Mun, J. J. Ehrhardt, J. Lambert and C. Madic, *Appl. Surf. Sci.*, 2007, **253**, 7613–7621.
38 A. Foelske, O. Barbieri, M. Hahn and R. Kötz, *Electrochem. Solid-State Lett.*, 2006, **9**, A268.
39 B. E. Conway, *J. Electrochem. Soc.*, 1991, **138**, 1539.
40 H. Xia, Y. Shirley Meng, G. Yuan, C. Cui and L. Lu, *Electrochem. Solid-State Lett.*, 2012, **15**, A60–A63.
41 E. Barsoukov and J. R. Macdonald, *Impedance Spectroscopy: Theory, Experiment, and Applications*, John Wiley & Sons, Inc., Hoboken, NJ, USA, 2005.
42 J. Bisquert, G. Garcia-Belmonte, F. Fabregat-Santiago, N. S. Ferriols, P. Bogdanoff and E. C. Pereira, *J. Phys. Chem. B*, 2000, **104**, 2287–2298.
43 J. Bisquert, *J. Phys. Chem. B*, 2002, **106**, 325–333.
44 F. Fabregat-Santiago, J. Bisquert, G. Garcia-Belmonte, G. Boschloo and A. Hagfeldt, *Sol. Energy Mater. Sol. Cells*, 2005, **87**, 117–131.
45 M. Toupin, T. Brousse and D. Bélanger, *Chem. Mater.*, 2004, **16**, 3184–3190.
46 S. Ardizzone, G. Fregonara and S. Trasatti, *Electrochim. Acta*, 1990, **35**, 263–267.
47 J. Wang, J. Polleux, J. Lim and B. Dunn, *J. Phys. Chem. C*, 2007, **111**, 14925–14931.
48 W. Yan, T. Ayvazian, J. Kim, Y. Liu, K. C. Donavan, W. Xing, Y. Yang, J. C. Hemminger and R. M. Penner, *ACS Nano*, 2011, **5**, 8275–8287.
49 J. Duay, S. A. Sherrill, Z. Gui, E. Gillette and S. B. Lee, *ACS Nano*, 2013, **7**, 1200–1214.

